Coupled Sea Ice–Mixed Layer Simulations for the Southern Ocean

ACHIM STÖSSEL AND PETER LEMKE[1]

Max-Planck-Institut für Meteorologie, Hamburg, Federal Republic of Germany

W. BRECHNER OWENS

Woods Hole Oceanographic Institution, Woods Hole, Massachusetts

A coupled sea ice–mixed layer–pycnocline model for the Weddell Sea (Lemke et al., this issue; Owens and Lemke, this issue) is extended to the entire sea ice area around the Antarctic continent. The monthly atmospheric forcing and the annual oceanic forcing are specified from climatology. Sensitivity runs were performed with a fixed mixed layer, without snow cover, with a different ice strength constant (P^*) and a varying e-folding constant for the closing of leads (h_0), without dynamics, and without ocean currents. Since the atmospheric forcing fields, although derived from large, historical data sets, differ considerably depending on the analysis technique, alternative wind, temperature, and precipitation forcing has been applied. Finally, the model has been forced with mean monthly winds supplemented by stochastic variations representing short-term variability. The model results are compared with analyses of satellite data as well as with single measurements, and with simulation results from earlier models.

1. INTRODUCTION

The winter sea ice extent around the Antarctic continent covers an area of almost the size of the U.S.S.R. During summer this large area shrinks to less than 20% of the maximum extent. This strong climatic signal has a significant influence on the Earth's surface albedo and the exchange of heat, moisture, and momentum between atmosphere and ocean.

In many general circulation models (GCMs), the simulation at high latitudes is rather unsatisfactory [e.g., *Loewe*, 1989]. A contributing factor to this problem could be the poor description of sea ice within those models. In atmospheric GCMs (AGCM) sea ice represents the lower boundary condition of the model and is normally treated as a slab of uniform thickness, the edge of which is determined either from climatology or from real-time observations. Oceanic GCMs (OGCM) are usually coupled to simple thermodynamic sea ice models to describe the salt balance, and hence the deep water production, in polar regions. These models often include an advection scheme but generally neglect sea ice dynamics.

To improve their performances in polar regions, GCMs should include more sophisticated sea ice models. Especially in the Southern Ocean the inclusion of realistic sea ice dynamics is important to properly describe the interaction of low ice concentration, areas of thin ice, and polynyas, with the atmospheric and oceanic circulation. Such attempts have recently been made with an OGCM (J. M. Oberhuber, A simulation of the Atlantic circulation with a coupled sea ice–isopycnal general circulation model, submitted to *Journal of Physical Oceanography*, 1990) and an AGCM (P. Loewe, personal communication, 1988).

The only other dynamic-thermodynamic simulation of the entire Antarctic sea ice cover has been carried out by *Parkinson and Washington* [1979]. The thermodynamic part of that model consists of heat balance equations for open water, ice without snow, and ice with snow, respectively. Ice velocities are calculated without regard for conservation of momentum, as described by *Owens and Lemke* [this issue] (hereinafter referred to as OL). The sea ice drift is rather small compared to observations, and the resulting thickness pattern differs little from those obtained from purely thermodynamic models. The atmospheric forcing consisted of mean monthly climatological values [*Taljaard et al.*, 1969], whereas the geostrophic currents were derived from annual means. The oceanic heat flux was kept constant in time and space.

As a further step towards a coupled atmosphere–sea ice–ocean GCM, the dynamic-thermodynamic sea ice model originally used by *Hibler and Ackley* [1983] for the Weddell Sea, which was recently modified to include an active oceanic mixed layer [*Lemke et al.*, this issue] (hereinafter referred to as LOH), has been extended to the entire Southern Ocean.

The next section briefly describes the model, its domain, and the derived quantities. The forcing fields are discussed in section 3. The results (section 4) are presented in four parts: (1) the standard run, (2) the sensitivity to important model parameters and to simplifications, (3) the response to alternative climatological forcing fields, and (4) the response to wind forcing with daily variability. Finally, conclusions and recommendations for future experiments are given in section 5.

2. OUTLINE OF THE MODEL

2.1. Sea Ice

The sea ice model used in this study is based on *Hibler* [1979]. It basically consists of an interaction between the momentum balance and the continuity equations of ice thickness and of ice compactness. The essential feature of

---

TABLE 1. Characteristics of Data Sets Used

Data Set/Source	Characteristics	Spatial Resolution, $\Delta\Phi \times \Delta\lambda$	Temporal Resolution	Forcing Variables
Taljaard et al. [1969]	southern hemisphere climatology	5° × 5°	monthly	air temperature; dew point temperature; geostrophic wind
Hellerman and Rosenstein [1983]	world ocean surface analysis, climatology	2° × 2°	monthly	wind stress
Oort [1983]	global analysis, climatology	2.5° × 5°	monthly	air temperature; standard deviation of wind components
Gordon and Baker [1982]	Southern Ocean hydrographic data	1° × 2°	annual	seawater density; deep ocean temperature; deep ocean salinity
van Loon [1972]	southern hemisphere total cloudiness	zonal averages	semiannual	cloud coverage
Tchernia [1980]	Southern Ocean estimates	zonal averages	annual	precipitation
Jaeger [1976]	global climatology	5° × 5°	monthly	precipitation

this model is the formulation of a viscous-plastic ice rheology which is introduced to determine the internal ice stresses in the momentum equation. The thermodynamic part of the model consists of a heat balance equation for ice-free and ice-covered water similar to *Parkinson and Washington* [1979] and enters together with the dynamic part in the continuity equations for sea ice mass and concentration. An additional continuity equation for snow thickness has been introduced according to OL. Additionally, creation of extra open water due to shear deformation and a seven-level ice thickness description for a differential determination of the growth rates in the ice covered part of a grid cell have been adopted, both following *Hibler* [1984].

2.2. Mixed Layer

In order to determine the vertical oceanic heat flux the one-dimensional mixed layer–pycnocline model of *Lemke* [1987] has been coupled to the sea ice model. The essential feature of the mixed layer model is the prognostic calculation of mixed layer depth, temperature, and salinity as well as the exponentially shaped profiles of the thermocline and halocline as a function of ice production and ice velocity. The calculations are based on conservation of heat and salt, potential energy considerations, and a parameterization for the entrainment fluxes. An overview of both the sea ice and the mixed layer model equations is given in LOH and OL.

2.3. Model Domain

The coupling of the two models follows LOH and OL. Additionally the horizontal stresses and advection terms in the model include metric factors [*Arakawa and Lamb*, 1977] so that it can be run alternatively in cartesian or in spherical coordinates.

In order to expand the model domain around the Antarctic continent the Weddell Sea grid used in LOH and OL was extended to a spherical grid for the latitudinal band 50°S–80°S with latitudinal and longitudinal mesh sizes of $\Delta\phi$ = 2.5° ($\simeq$ 277.8 km) and $\Delta\lambda$ = 5° ($\simeq$ 234.8 km at ϕ = 65°S). The land points were masked out according to the latest bathymetric chart. Shelf ice grid cells were treated as land points. Cyclic boundary conditions were introduced at the east-west boundaries.

2.4. Derived Quantities

The heat fluxes of shortwave and long-wave radiation are treated following *Parkinson and Washington* [1979]. Sensible and latent heat fluxes are derived from standard formulas, where the transfer coefficients are chosen to be 1.75 × 10^{-3} and where humidity is derived from dew point temperature. The stresses at the air/ice and water/ice interfaces are calculated with standard quadratic bulk formulas as given, e.g., by *Hibler and Ackley* [1983], where the drag coefficients are taken to be 1.2 × 10^{-3} and 5.5 × 10^{-3}, respectively, and the turning angles were chosen as 25°.

The geostrophic currents were calculated from the dynamic topography referenced to 1000 m by the standard geostrophic method. The temperatures and salinities at the base of the second oceanic layer defined at 500 m depth are specified as given boundary conditions.

3. Forcing Data

Table 1 shows the different data sets with their characteristics and the variables used to force the coupled model. Since, for the same variable, the forcing value itself may vary considerably depending on the data source and analysis technique, different forcing fields were employed to test their influence on the simulations.

The data set of *Taljaard et al.* [1969], although somewhat old, still appears to be the most consistent one for the Southern Ocean (H. van Loon, personal communication, 1988). Following *Parkinson and Washington* [1979] and *van Ypersele* [1986], the atmospheric variables temperature, humidity, and geostrophic wind were derived from the same data set and used as standard atmospheric forcing for the present model.

The surface wind stress data from *Hellerman and Rosenstein* [1983] which are derived from observed surface wind velocities, as well as surface air and seawater temperature have also been used to give an alternative wind forcing. The latter variables were necessary to determine the stability dependent drag coefficient in the calculation of the stresses. For polar regions neutral stability was assumed which eliminated any direct feedback between ice cover and static stability within the atmospheric boundary layer. Thus, if

there is open water or ice with low concentration or thin ice without snow cover a bias toward lower stresses may occur [*Hellerman and Rosenstein*, 1983]. Since observations in the Southern Ocean are rather sparse, especially in wintertime, the application of this wind stress data set is more critical than the pressure-derived winds of *Taljaard et al.* [1969], where air pressure measurements from shore stations are included.

A second data set of surface air temperature [*Oort*, 1983] has local differences in monthly mean values of up to 10°C compared to *Taljaard et al.* [1969]. This is mainly due to different analysis techniques which are crucial when the data sampling net is coarse. Temperature and humidity forcing for OGCMs with a combined data set of *Taljaard et al.* [1969] and the comprehensive ocean-atmosphere data set (COADS) [*Woodruff et al.*, 1987] yield more realistic deep water formation and meridional transport compared to a correspondent forcing with the *Oort* [1983] data set (J. M. Oberhuber and E. Maier-Reimer, personal communication, 1988). Since the COADS data are too sparse in the Southern Ocean [*Wright*, 1988], they were not used in the present study. For a combined data set of the COADS and *Taljaard et al.* [1969] data, which themselves are composed from different sources and periods, temperature data were almost consistent in the overlap region between 20°S and 30°S, supporting the quality of the *Taljaard et al.* [1969] data (J. M. Oberhuber, personal communication, 1988).

In the absense of any consistent, gridded cloudiness data for the Southern Ocean region, this variable was specified as a function of latitude according to *van Loon* [1972]. Satellite-derived data have not been used due to difficulties of identifying clouds over snow and ice-covered regions [*Stowe et al.*, 1989].

Similarly, the zonally averaged precipitation data of *Tchernia* [1980] was taken as part of the standard forcing data set. Alternatively, the precipitation grid point data from *Jaeger* [1976] were used, which show a high longitudinal and month to month variability in that region.

The dynamic topography, used to calculate the geostrophic currents, was derived from the ocean density stratification given in the climatic data set of *Gordon and Baker* [1982]. Temperature and salinity at the base of the second oceanic layer (T_b, S_b) were extracted from the same data set.

All climatological grid point forcing data were spatially interpolated to the staggered 2.5° × 5° grid, weighted with geographic distances. Additionally, the monthly mean values were interpolated linearly in time to give "daily" values for the one day time step used in the numerical integration assuming the midmonth value to be that of the monthly mean. The dynamic topography as well as the geostrophic currents were calculated before interpolating spatially to obtain a smooth forcing field.

4. RESULTS

4.1. Standard Run

In the standard simulation the full dynamic-thermodynamic sea ice model is coupled to the prognostic mixed layer model with an exponential pycnocline (LOH). Snow is included according to OL using snowfall rates determined from precipitation data of *Tchernia* [1980]. The numerical parameters of the sea ice model are set to the original values
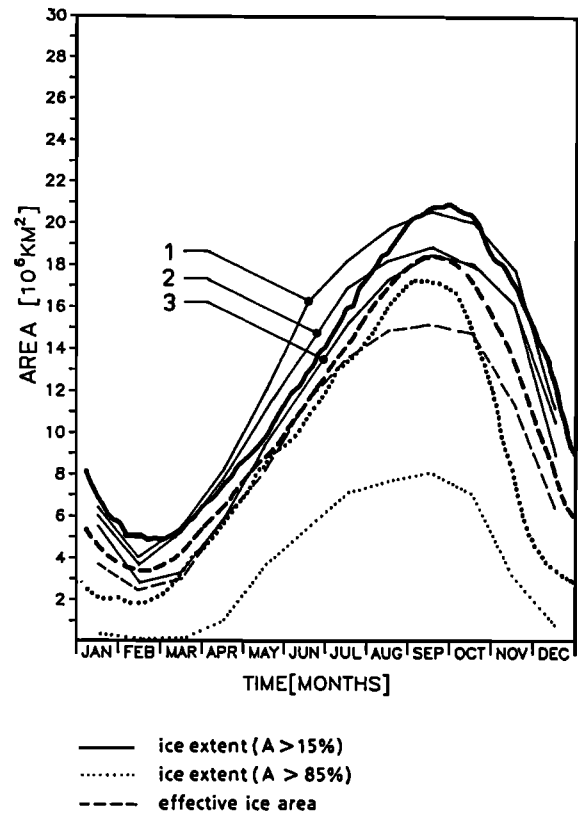

Fig. 1. Seasonal cycles of simulated (heavy lines) and observed (thin lines) ice extents and effective ice area. The simulation results are from the standard run. The observed data are composed from monthly means according to *Zwally et al.* [1983] and *Lemke et al.* [1980] (for details see text).

of *Hibler* [1979]. The temperature and wind forcing is taken from the *Taljaard et al.* [1969] data set. The results shown are from the sixth year of simulation, where ice extent and ice volume are nearly cyclostationary. The initial conditions (January 1) were a linear latitudinal decrease from an ice thickness (h_i) of 2 m, an ice compactness (A) of 100% and a snow thickness (h_s) of 0.5 m at ϕ = 80°S to h_i = A = h_s = 0 at ϕ = 65°S, and ice velocity components (u, v) of 0.05 m/s, a mixed layer thickness (h) of 60 m, a mixed layer salinity (S) of 33.3, a mixed layer temperature (T) at the freezing point, a thermocline thickness (d_T) of 70 m, and a halocline thickness (d_s) of 20 m, everywhere.

Figure 1 shows the seasonal cycle of simulated (heavy line) and observed (thin line) ice extent and effective ice area. The ice extent is defined as the sum of grid cells containing ice multiplied by their areas. Two categories of ice extent are compared: In the first case the areas of all grid cells where the ice compactness A > 15% are summed (heavy solid line), whereas in the second case only those grid cells where A > 85% are included (heavy dotted line). The effective ice area (heavy dashed line), on the other hand, is defined to be the sum of the grid cell areas multiplied by their actual ice concentrations.

The observed seasonal cycles for ice extent A > 15% come from two sources: two curves are from *Zwally et al.* [1983], one showing monthly mean values of the year 1976 (2) and the other one (1) showing 4-year average values of the monthly means from 1973–1976. The third curve (3) is taken from *Lemke et al.* [1980] representing the annually
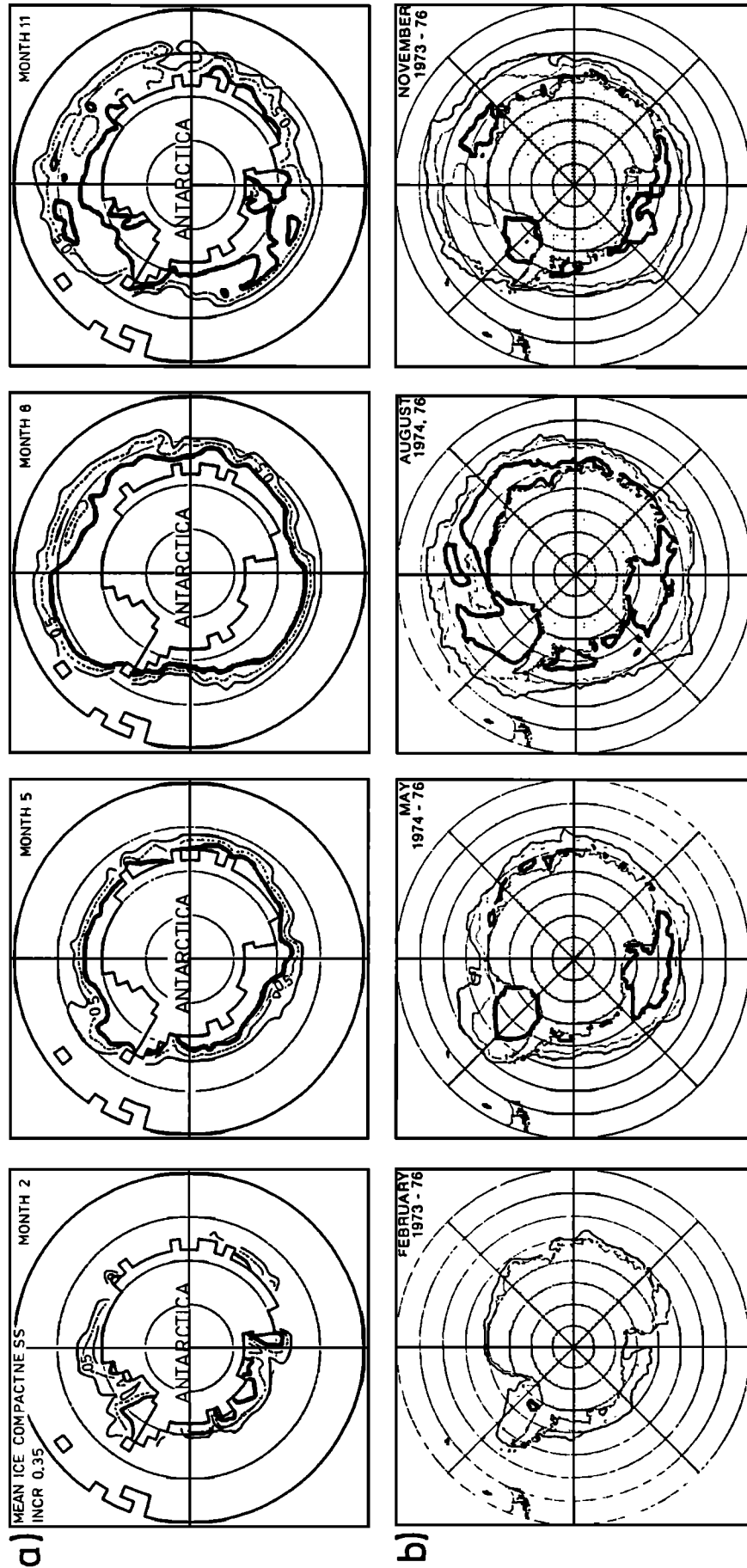
Fig. 2. Contours of (a) simulated and (b) observed ice compactness for each midseason month. The simulated contours display the mean ice compactness of a month, while the observed contours show mean monthly values averaged over the years indicated according to Zwally et al. [1983].

15.0% BOUNDARY   50.0% BOUNDARY   85.0% BOUNDARY

averaged ice cover for the period 1973 to 1979. The thin dotted curve shows the observed ice extent $A > 85\%$ and the thin dashed curve represents the observed effective ice area. Both are 4-year averages for the years 1973–1976 according to Zwally et al. [1983].

Generally, the simulated ice extent for $A > 15\%$ compares quite well with the observations, although the simulated ice extent in summer is somewhat higher than observed. For the effective ice area the shape of the simulated seasonal cycle agrees well, too, but the magnitude of the effective winter ice area is about 3×10^6 km^2 too large. The discrepancy is even higher for the ice extent $A > 85\%$. It appears that the model generates too high compactnesses. One reason may be the low value of h_0 (see section 4.2.4) which tends to close leads and polynyas too fast. Another reason is the fact that the wind forcing is a linear interpolation of monthly values (see section 4.4). Thus, grid cells with high ice concentration can develop rather easily since ice cannot be dispersed with the daily variability. Finally, the results are highly dependent on the quality of the atmospheric forcing fields, as will be shown in section 4.3.

The seasonal variation of the areal distribution of sea ice compactness is shown in Figure 2. Figure 2a displays the simulated mean ice compactness of every midseason month, whereas Figure 2b shows the mean monthly ice compactness for the midseason months averaged for the years indicated, as observed by satellite [Zwally et al., 1983]. The seasonal evolution of the areal distribution of sea ice is well simulated, though in summertime the modeled ice extent is too large within the sector 30°W to 20°E, and the ice between 150°E and 165°E, i.e., north of Oates Land, is shifted to the east of Victoria Land. The discrepancy in the area of high ice compactness is clearly visual in the maps, too.

One should bear in mind, however, that uncertainties in the determination of ice concentration from satellite data may occur due to errors in both the brightness temperature and the estimated surface temperature of ice or snow, respectively. The ice extent $A > 85\%$ is most sensitive to those errors because the integral area of an error band at $A = 85\%$ is much larger than at $A = 15\%$ (for the same error), especially in wintertime [Zwally et al., 1983].

Additionally it should be noted that the observed ice extent for $A > 85\%$ is underestimated due to the 4-year averaging and also due to the monthly time averaging of each map element (pixel) before the areal summation is carried out (Figure 1). Assuming that the ice edge is sharp, i.e., ice concentration is either 100% or 0%, the natural meandering of the ice edge during one month would produce mean values between 100% and 0%, for all pixels within the meandering band, while, in an ideal case, daily pixel values would adopt only 100% or 0%, respectively, if the pixels were infinitesimally small and no ice movement occurred within one day. Thus, areal summation of daily pixel areas would increase the area of high ice concentration by half the area of the meandering band. For this case the application of the Zwally et al. [1983] averaging method would yield the probability of occurrence of highly concentrated ice.

The latter discrepancy is partly compensated for by the fact that the model resolution is about 100 times coarser than the pixel resolution of the satellite data (30 × 30 km). Nevertheless, it is not adequate to employ the same averaging procedure as Zwally et al. [1983] for the model results, because of the lack of daily variability (see section 4.4). In
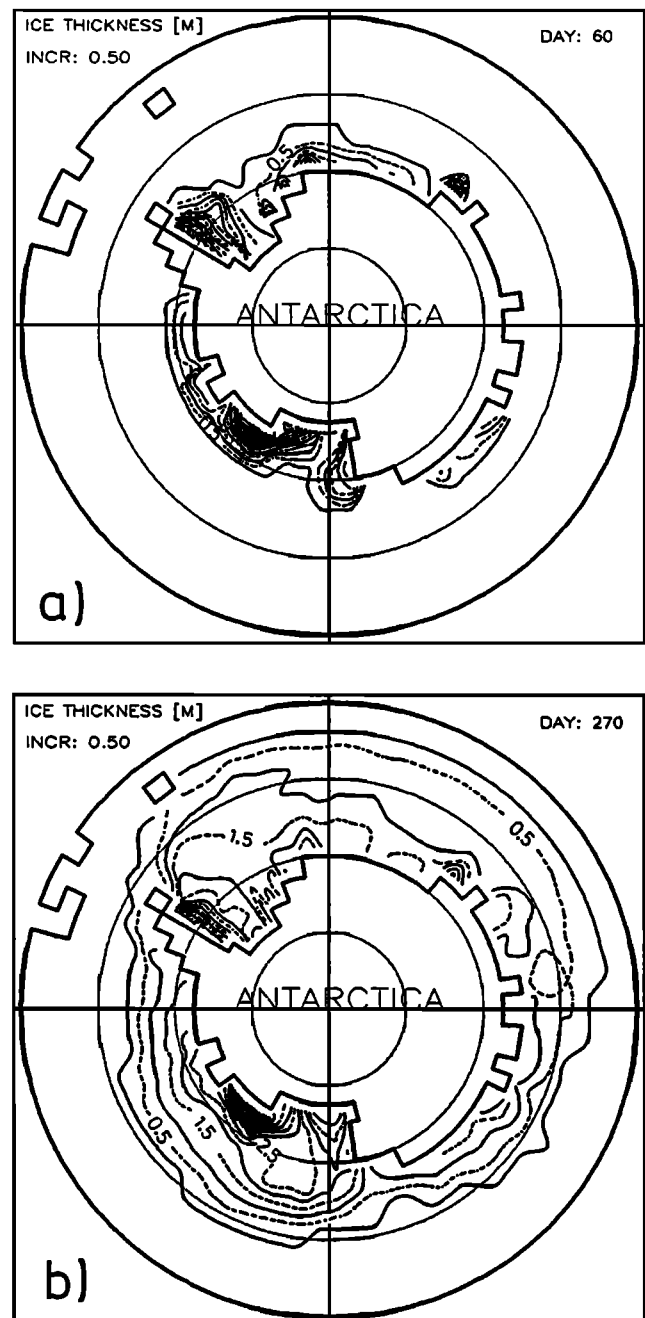

Fig. 3. Ice thickness contours of the standard run for the (a) minimum and (b) maximum ice extent.

fact, real-time ice concentrations derived from operational ice charts (Navy/National Oceanic and Atmospheric Administration Joint Ice Center) for selected days show a much more distinct ice edge and thus better agreement with the model results for the area of high ice concentration.

In Figure 3 maps of ice thickness are shown for the minimum (Figure 3a) and maximum (Figure 3b) ice extent at the end of February and the end of September, respectively. The thickest ice is encountered at the eastern side of the Antarctic Peninsula and at the eastern side of the Ross Sea. In wintertime most of the sea ice area has thicknesses between 0.5 and 1.5 m. This is in reasonable agreement with the few observations available [e.g., Wadhams et al., 1987].
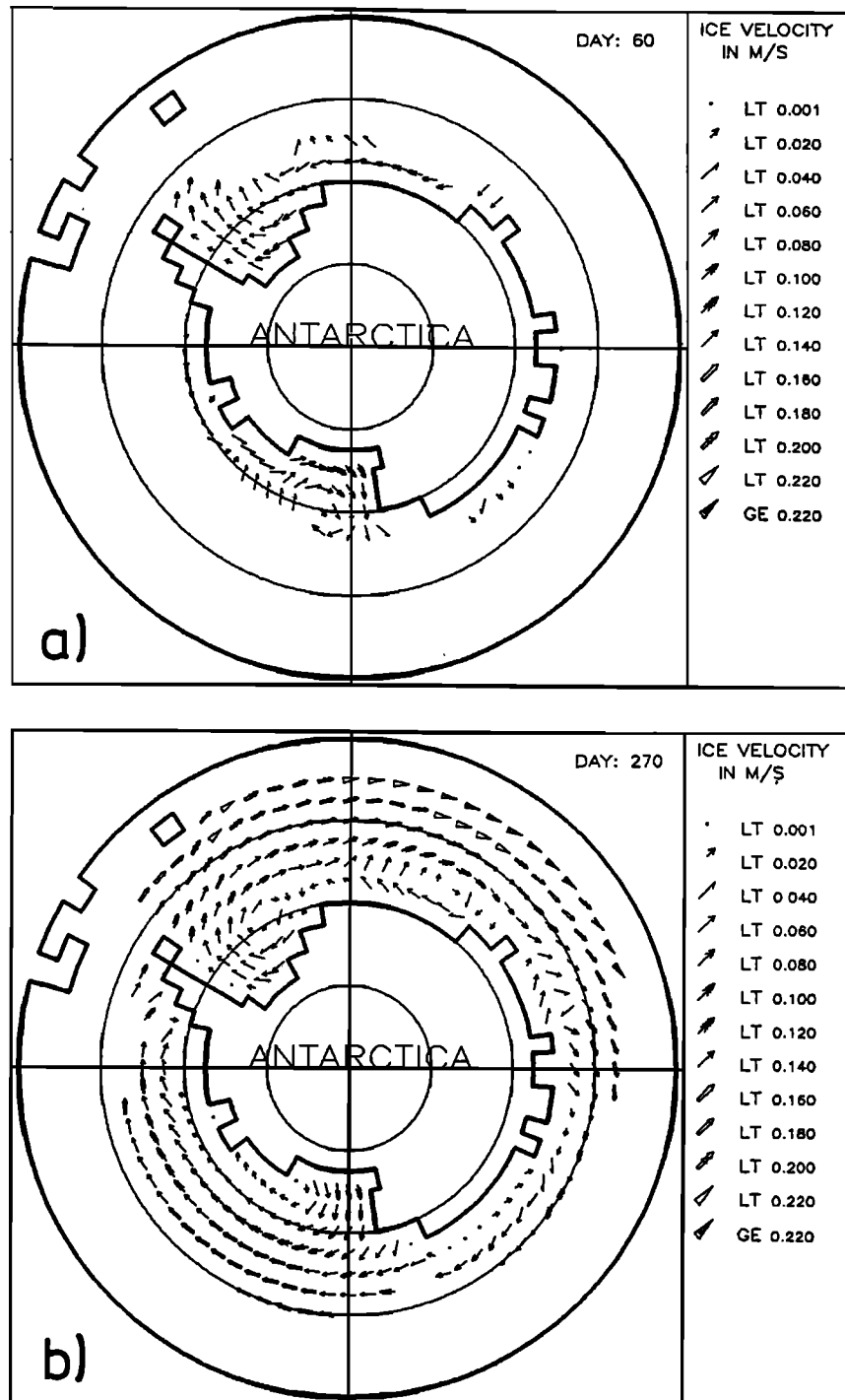
Fig. 4. Ice velocities of the standard run for the (a) minimum and (b) maximum ice extent. LT and GE in the velocity arrow scale denote "less than" and "greater than or equal to," respectively.

Comparing the observed ice thickness of 0.5–0.6 m along the Greenwich meridian with Figure 3 it should be noted that the observed thicknesses are obtained from ice drilling in (thermodynamically grown) level ice, whereas the model results represent the mean ice thickness of one grid cell, including ice mass stored in pressure ridges. Since ice compactness is usually more than 90%, the fraction of the open water remains small. Coastal polynyas occur at the southeastern

Weddell Sea and at the southwestern part of the Ross Sea, coinciding with satellite data [Zwally et al., 1983].

The corresponding ice velocities are displayed in Figure 4 with maximum speeds of up to 24 cm/s at the winter ice edge at about 55°S. The Weddell Sea gyre is well pronounced as is the offshore ice drift in the southern Weddell and Ross Seas. Both locations of offshore ice drift agree well with observations and coincide with the locations of maximum ice pro-
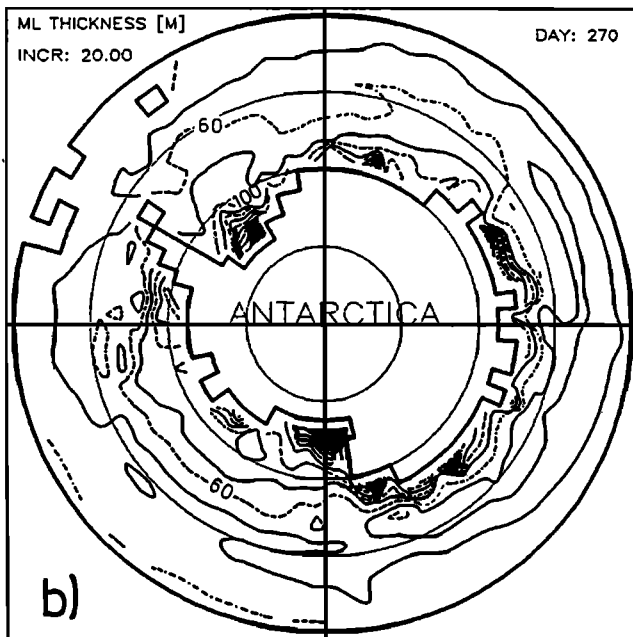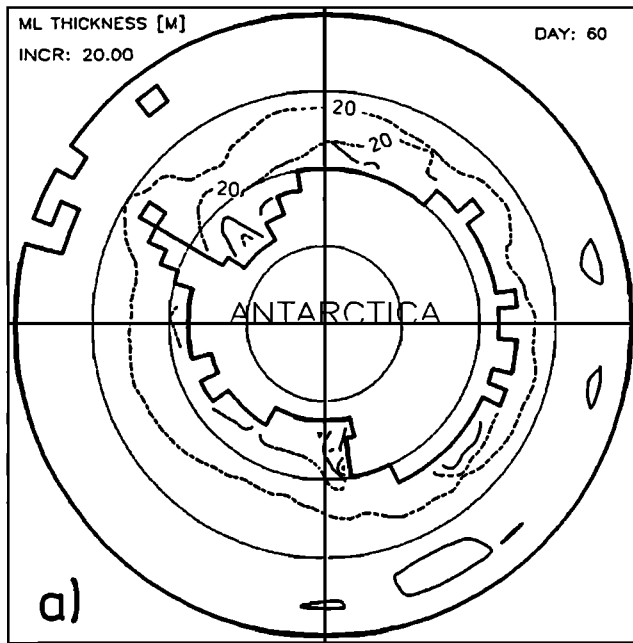
Fig. 6. Monthly mean oceanic heat flux of the standard run for August. The minimum contour line is 2 W/m².

Fig. 5. Mixed layer thickness contours of the standard run for the (a) minimum and (b) maximum ice extent.

duction, deep convection, and highest oceanic heat flux during the winter season. This can be seen from the wintertime mixed layer depth which is shown in Figure 5b. Generally the mixed layer is 40–80 m deeper in winter than in summer (Figure 5a). In regions of high ice production the mixed layer depth reaches several hundred meters. The monthly mean oceanic heat flux (Q_o) for August is displayed in Figure 6. Its maxima occur in the ice production areas and also at the ice edge during fall and early winter when the freezing rates and accordingly the entrainment velocities are large. From the middle of November till the end of January Q_o is negligible, whereas from the middle of March till the middle of September the monthly and spatial means vary
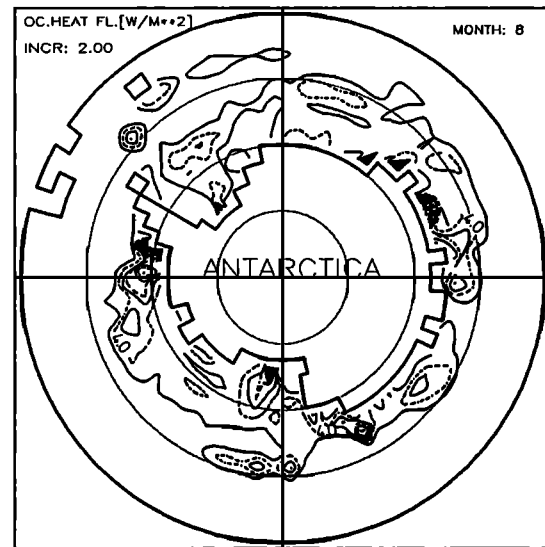
between 3.8 and 4.5 W/m². During this time temporal and local maxima of up to 60 W/m² may occur.

In order to demonstrate the convergence to cyclostationary conditions, Figure 7 shows the seasonal cycles of ice extent (Figure 7a) and ice volume (Figure 7b) for the first six years of simulation. The ice extent is in equilibrium after the fourth year of simulation, whereas the ice volume appears to be in equilibrium at the sixth year of simulation. While the ice coverage quickly adjusts to the forcing fields without marked delays, the ice thickness takes longer to reach equilibrium. This is mainly due to dynamic effects, e.g., opening of leads causing new ice production, or continuous ice ridging, when ice is not yet thick enough and thus the ice strength still too weak to resist the pressure. The latter is especially true under strong, persistent wind stress conditions toward a convergent coastline, e.g., a bay. Additionally, wind variability, too, influences the equilibrium of the total ice volume (see section 4.4). However, equilibrium of the ice thickness can also be delayed due to thermodynamic processes, which is the case when the snow cover is not accounted for (see next section).

4.2. Sensitivity Runs

4.2.1. Fixed mixed layer.
In order to demonstrate the effect of the variable mixed layer model, a test run has been performed with a mixed layer depth of 60 m fixed in time and space, and a constant vertical oceanic heat flux of 3.15 W/m² which is the spatial and temporal average value of the calculated heat flux in the sixth simulation year of the standard run. The results correspond to those of a similar experiment in LOH (shown there in Figure 3). For the Southern Ocean, compared to the standard case, the fixed mixed layer case shows a temporal delay in the increase of ice extent until mid July followed by an increased ice advance which finally leads to about 1×10^6 km² more ice in wintertime (not shown). The seasonal cycle of ice volume is quite similar in shape and magnitude to the standard run, as are the ice thickness contours.
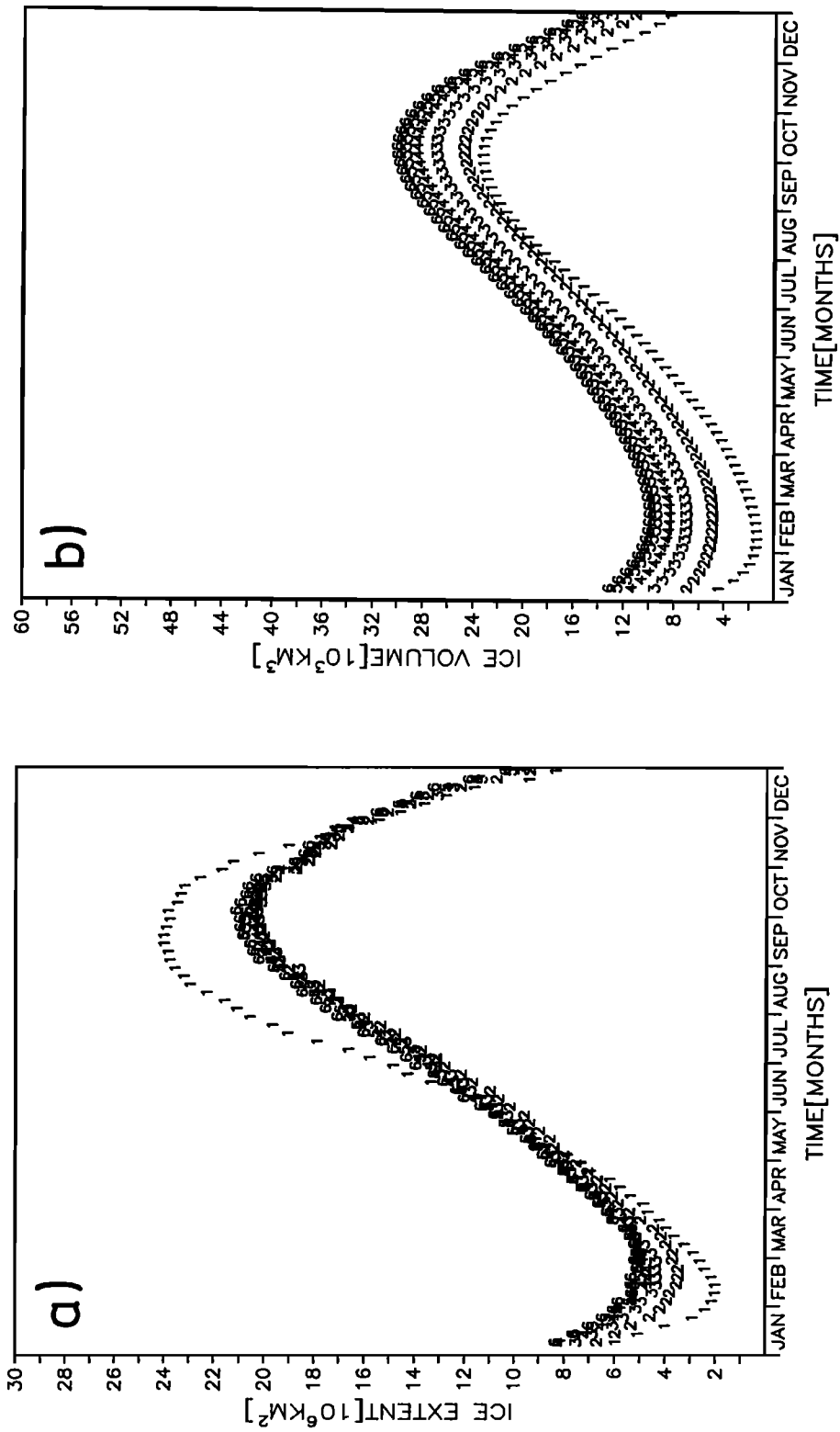
Fig. 7. Seasonal cycles of (a) ice extent and (b) ice volume for six consecutive simulation years of the standard run starting from the standard initial conditions.

4.2.2. No snow. In the standard experiment the snow thickness was simulated prognostically. Its depth varied between 0 and 50 cm on the first year sea ice, increasing continuously with advancing season until the end of October (maximum values of 70 cm), and to a certain extent also with advancing latitude. This feature is in agreement with observations from *Wadhams et al.* [1987]. Nevertheless, since the model doesn't include snow ice formation, which might reduce snow thickness, this variable may be slightly overestimated.

In order to demonstrate the effect of the snow layer on ice thickness, a test run without snow treatment was performed similar to OL (shown there in Figure 1). For the Southern Ocean, the seasonal cycle of ice extent is higher in magnitude by about 5×10^6 km^2 in spring and 2×10^6 km^2 during the rest of the year (not shown). The increase is even larger for the ice volume. These results show that it is essential to include a snow cover in sea ice models. This is especially true for first year sea ice which is relatively thin compared to the effective snow cover (snow thickness multiplied with the ratio of the thermal conductivities of sea ice and snow).

4.2.3. Higher ice strength. Another sensitivity experiment was performed to examine the effect of the ice strength parameter P^*. This is different from the correspondent experiment in OL in the sense that in this study the original value of 5×10^3 N/m^2 of *Hibler* [1979] has been used for the standard case, because the atmospheric forcing consists of monthly means. The use of daily atmospheric forcing variables was the reason for *Hibler and Ackley* [1983] to increase P^* to 5.5 times the original value. Figure 8 shows the effect of this higher ice strength on the ice thickness distribution in summer and winter. While the influence on the ice extent is negligible, the ice thickness pattern differs considerably compared to the standard case. In the Weddell Sea the ice convergence is reduced with a maximum ice thickness of 6 m in the southwestern corner, compared to the standard case where the maximum was more than 7 m at the northwestern part. In the eastern part of the Ross Sea, the ice thickness is reduced from 7.5 m to 4.5 m. The effect of the higher P^* value is even more obvious for the ice velocities, which are shown in Figure 9. In wintertime the ice in the Weddell Sea is almost stagnant and in other parts the velocity is reduced by up to 4 cm/s. The seasonal cycle of ice extent (not shown) is almost identical to the standard one, whereas the ice volume is reduced by about 2×10^3 km^3 during the entire seasonal cycle. Following the reasoning of *Hibler and Ackley* [1983] the standard case with smaller P^* appears to be appropriate. In fact, the higher P^* experiment seems to approach a "thermodynamics-only" case (see section 4.2.5.).

4.2.4. Slower lead closing. Figure 10 shows the seasonal cycles of ice extent and effective ice area for a test run with $h_0 = 1.0$ instead of 0.5. Compared to the standard run it can be seen that the extent of highly concentrated ice is about 2×10^6 km^2 smaller during fall and winter, and thus somewhat closer to the "observations," shown in Figure 1. The total ice volume (and thus ice thickness), on the other hand, increased by about 25%, which is commensurate to the results of OL. This indicates that h_0 is not the appropriate parameter to reduce the high ice compactness and, at the same time, keep the high ice thickness at the level of the standard run, which agrees rather well with observations [*Budd*, 1987; *Wadhams et al.*, 1987].
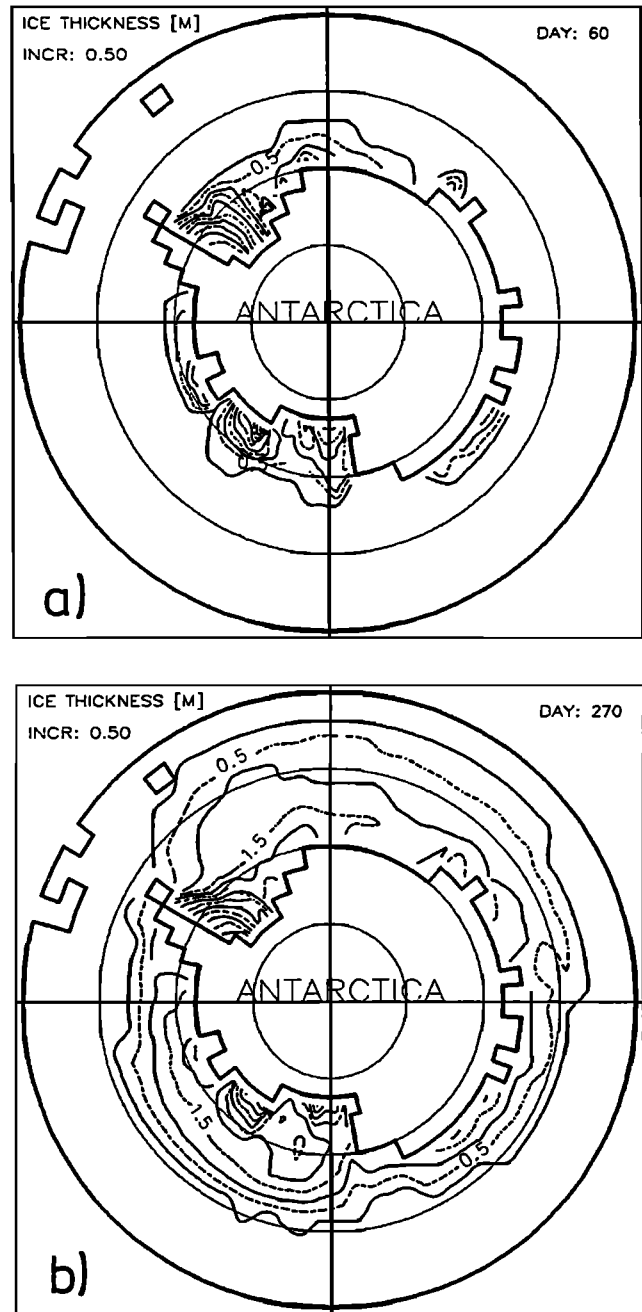

Fig. 8. Ice thickness contours from a test run with a higher P^* value for the (a) minimum and (b) maximum ice extent.

4.2.5. No advection. To illustrate the influence of ice dynamics, a sensitivity run without dynamics has been performed. Figure 11 shows the ice thickness contours for this "thermodynamics-only" case, which differs considerably from the standard experiment. The thickness contours follow the more or less zonally distributed atmospheric temperature forcing. The seasonal cycle is rather weak. South of 65°S hardly any differences occur between winter and summer. This is due to the fact that within this region the monthly mean temperature is below 0°C during the entire year while the solar radiation is not strong enough to reduce ice thickness effectively. On the other hand, little ice growth takes place during fall and winter. Since this could be
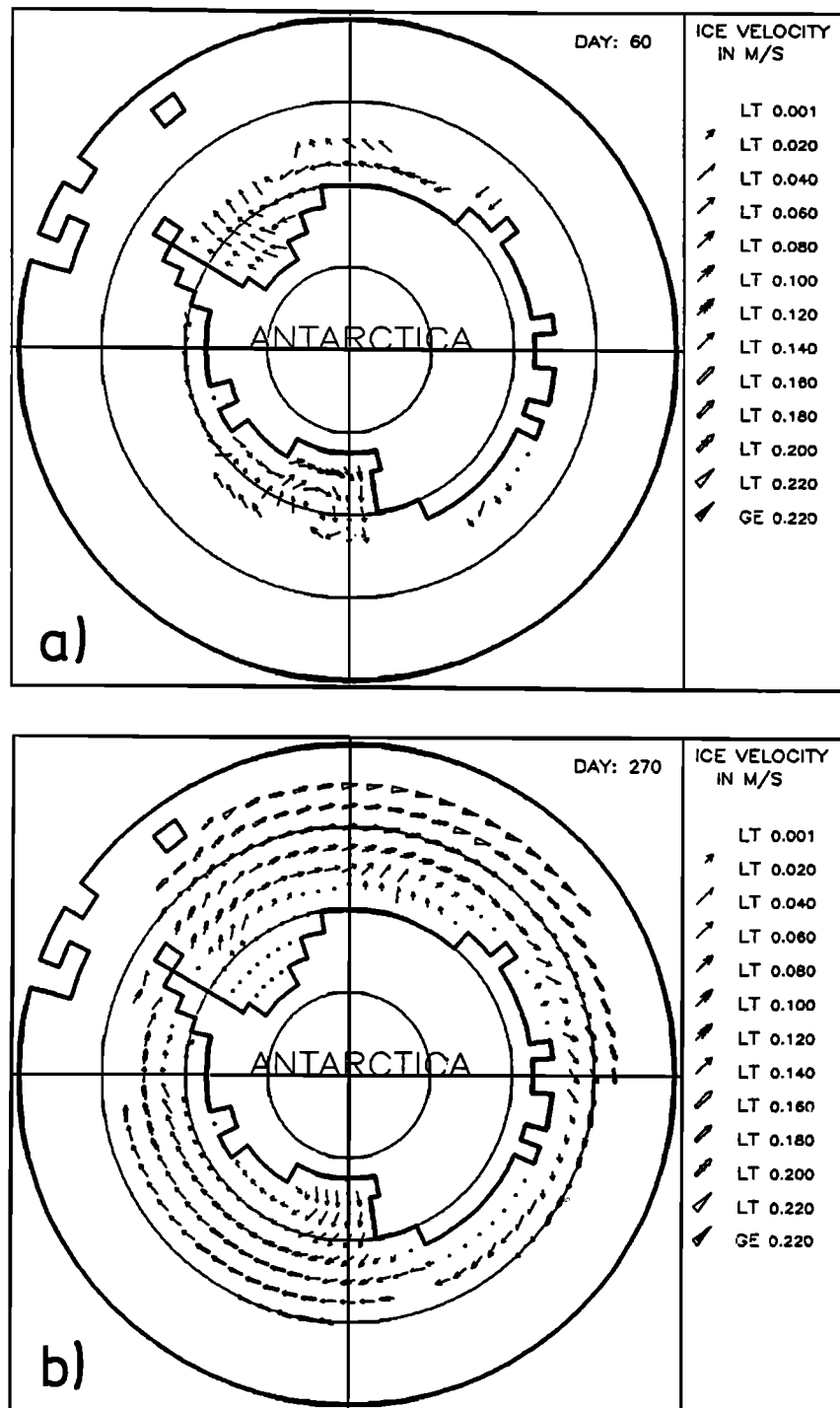
DAY: 60

ICE VELOCITY
IN M/S

LT 0.001
LT 0.020
LT 0.040
LT 0.060
LT 0.080
LT 0.100
LT 0.120
LT 0.140
LT 0.160
LT 0.180
LT 0.200
LT 0.220
GE 0.220

ANTARCTICA

a)

DAY: 270

ICE VELOCITY
IN M/S

LT 0.001
LT 0.020
LT 0.040
LT 0.060
LT 0.080
LT 0.100
LT 0.120
LT 0.140
LT 0.160
LT 0.180
LT 0.200
LT 0.220
GE 0.220

ANTARCTICA

b)

Fig. 9. Ice velocities for the days of (a) minimum and (b) maximum ice extent as simulated by a test run with a higher P^* value. LT and GE in the velocity arrow scale denote for "less than" and "greater than or equal to," respectively.

attributed to the snow, which has accumulated on the perennial sea ice to a few meters during the six simulation years, the "thermodynamics-only" experiment has been repeated without snow cover, showing no marked difference from the latter run for the seasonal cycle of ice extent and the seasonal amplitude of ice volume. However, the total ice volume was increased by about twice the magnitude of the previous run.

If, however, the prognostic mixed layer is replaced by a fixed mixed layer, the seasonal cycle of the ice extent can be increased depending on the specified constant oceanic heat flux. The results of such an experiment are displayed in Figure 12, where the oceanic heat flux was taken to be the annual (and spatial) means of the no-advection case with (1) snow and prognostic mixed layer, (2) the standard case, and (3) a value used by Crowley and Parkinson [1988]. For the
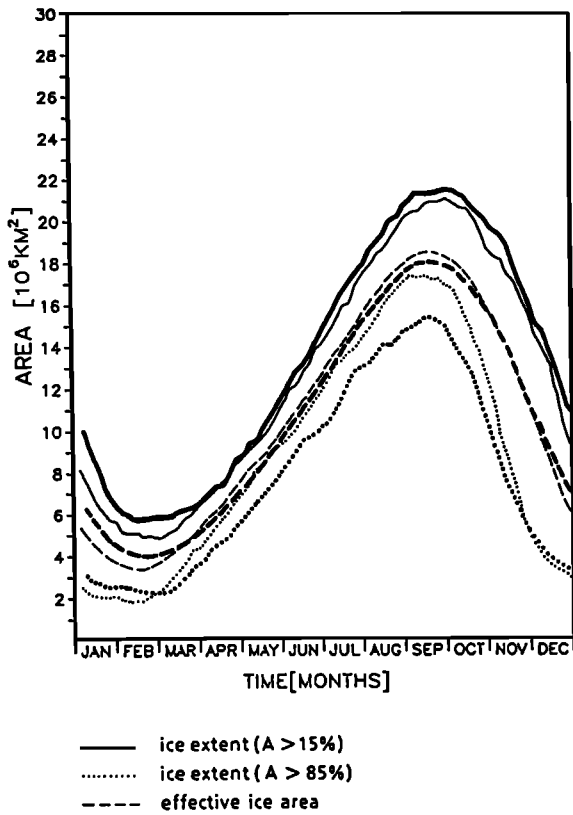
- ―――― ice extent (A >15%)
- ·········· ice extent (A > 85%)
- ― ― ― ― effective ice area

Fig. 10. Seasonal cycles of ice extent and effective ice area from a test run with a higher h_0 value (heavy lines) and from the standard experiment (thin lines).

Fig. 11. Ice thickness contours of a test run without sea ice dynamics for the (a) minimum and (b) maximum ice extent.

latter case, the amplitude of ice extent is almost the same as for the standard run. Since the ice dynamics were neglected, this apparent improvement, however, is deceptive, since it arises from an overestimation of the oceanic heat flux during summer and an underestimation during winter. Note that the ice volume is highly sensitive to the Q_o prescription in this experiment. The ice thickness pattern remains zonally symmetrical similar to the results of *Parkinson and Washington* [1979]. This demonstrates the importance of including an active mixed layer together with proper sea ice dynamics.

The results imply that the pronounced seasonal cycle of ice extent in the Southern Ocean is generated by ice dynamics, where ice is produced near the continent and transported to warmer regions (north of 65°S), where it is melted. This can also be seen in Figure 13, showing the net freezing rate integrated over the sixth simulation year of the standard run, with more thermodynamic ice growth than melt in the offshore areas of up to 3 m in the southern Weddell Sea and up to 5.5 m in the southern Ross Sea.

4.2.6. *No ocean currents.* Finally, an experiment neglecting the geostrophic currents in calculating the ice/water stress has been performed showing no significant differences compared to the standard run, except for some locations near the coast and north of 60°S. This confirms that the annual mean geostrophic currents exert almost negligible influence on the stress at the ice/water interface, which itself is mainly determined by the ice drift.
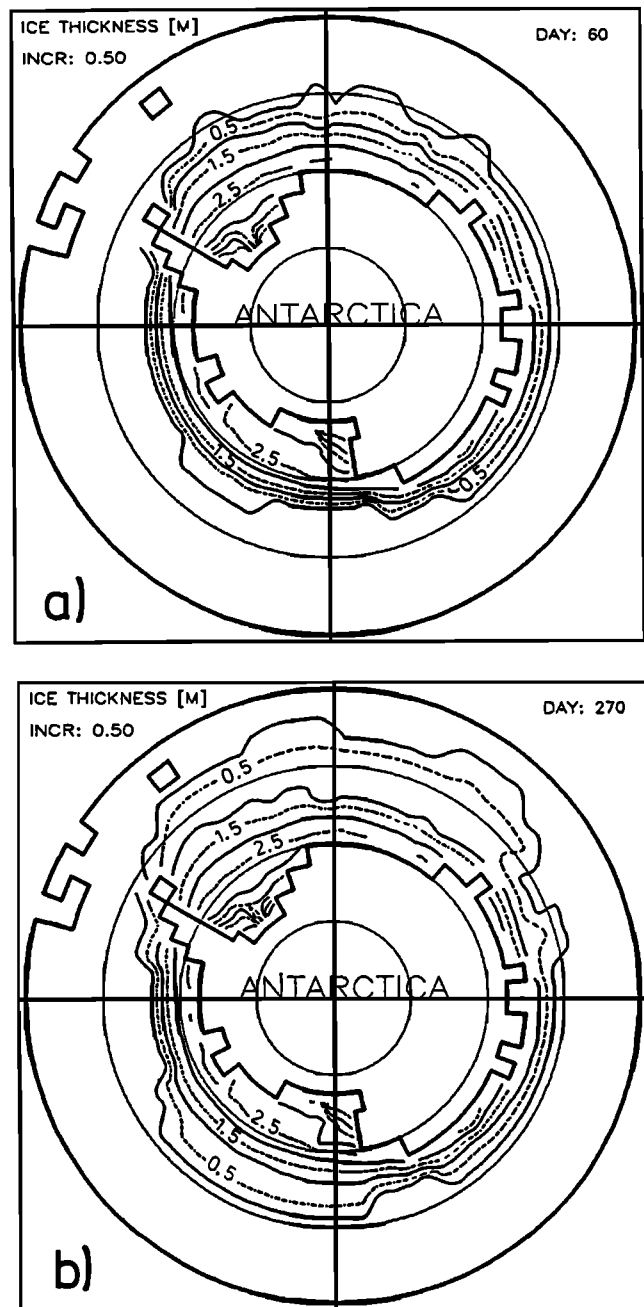
4.3. Alternatively Forced Experiments

4.3.1. *Wind.* In order to show the influence of different forcing fields on the distribution of sea ice, the standard run has been repeated with the wind stresses from *Hellerman and Rosenstein* [1983]. The seasonal cycles of ice volume and especially of ice extent (Figure 14, heavy lines) differ considerably from the standard results (thin lines): the seasonal cycle of ice extent is larger by about 5×10^6 km^2 with less ice in summer and more ice in winter. From mid April until mid August there is a rapid ice advance of about 5×10^6 km^2 per month compared to 3×10^6 km^2 per month in the standard experiment. For this case, the rates of advance and retreat are similar, in contrast to the standard
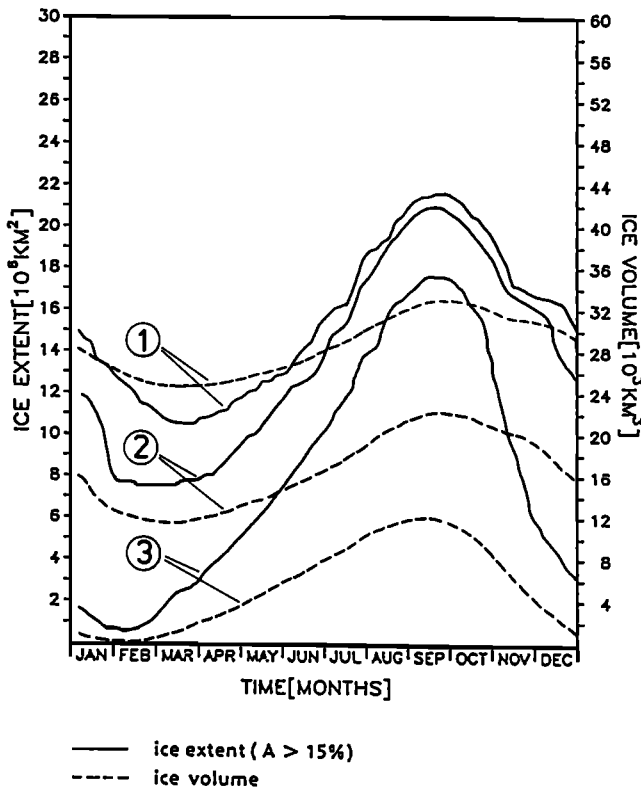
Fig. 12. Seasonal cycles of ice extent and ice volume from a sensitivity run without ice advection and with fixed mixed layer for three differently specified constant oceanic heat fluxes: (1) 0.5 W/m^2, (2) 3.1 W/m^2, and (3) 20.0 W/m^2.
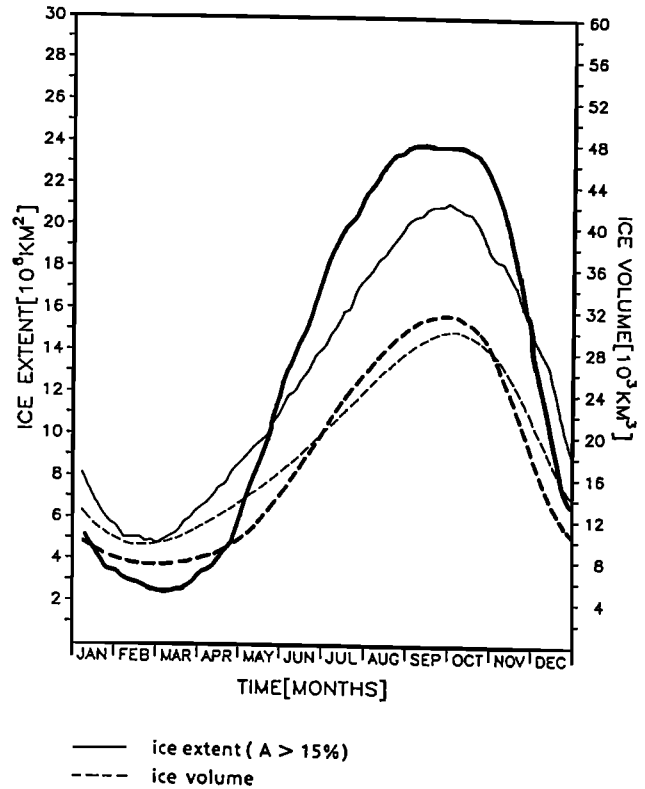

Fig. 14. Seasonal cycles of ice extent and ice volume from a simulation forced with winds from *Hellerman and Rosenstein* [1983] (heavy lines) and from the standard run (thin lines).

run, where the retreat is faster than the advance. A corresponding shift is apparent in ice volume with a larger seasonal cycle of about 4 × 10^3 km^3. The change in spatial ice thickness distribution (Figure 15) compared to the stan-
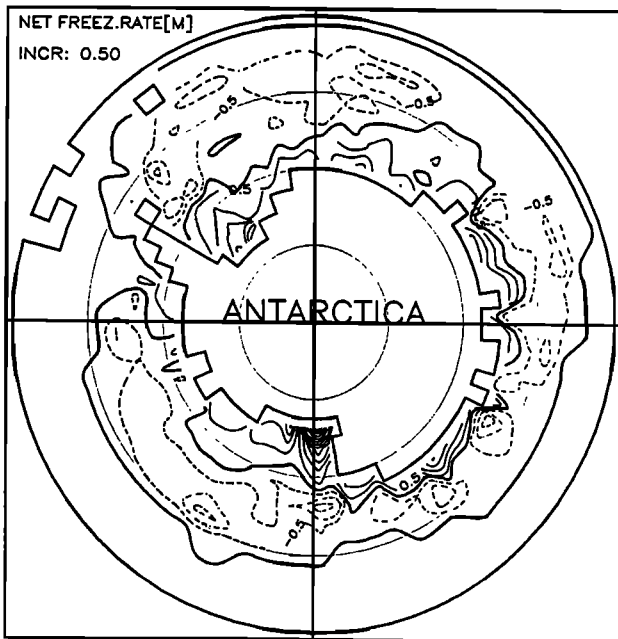

Fig. 13. Net freezing rates in equivalent meters of ice thickness for the sixth simulation year. Dashed lines show more ice melting than freezing, thin solid lines indicate the opposite.

dard experiment is large and is due to significant changes in the wind stresses, e.g., for September (Figure 16). In the *Taljaard et al.* [1969] data (Figure 16a) the Weddell Sea and Ross Sea gyres are well pronounced, and several smaller gyres with easterly winds along the coast are visible, whereas the *Hellerman and Rosenstein* [1983] wind stresses (Figure 16b) are more or less zonal. Since the winds are blowing steadily eastward the ice piles up against the west coast of the Antarctic Peninsula to about 12 m thickness and there is no ice convergence in the western Weddell Sea. Similarly, the zonal winds do not allow ice convergence in the region east of the Ross Sea (between 120°W and 150°W).

From these results we can infer that the sea ice distribution is most sensitive to the patterns of the wind stress which vary considerably depending on the analyses of surface wind or pressure fields in the Southern Ocean.

4.3.2. *Temperature.* Using an alternative temperature forcing field [*Oort,* 1983] modifies the results, also, although not as dramatically as the wind forcing shown above. South of 65°S this temperature field is generally somewhat warmer than the standard one. The modified response is especially apparent in the seasonal cycle of the total ice volume (Figure 17), which is up to 4 × 10^3 km^3 smaller than that of the standard experiment. The maximum ice extent occurs about half a month earlier and the summer ice extent is about 2 × 10^6 km^2 smaller, and thus closer to observations. Figure 18 indicates that the maximum ice thicknesses are up to 2 m lower and that the area of thicker ice ($h_i > 1$ m) is smaller compared to the standard case. Other variables, such as ice velocity and ice concentration, are not significantly different from the standard results. It should be mentioned here that
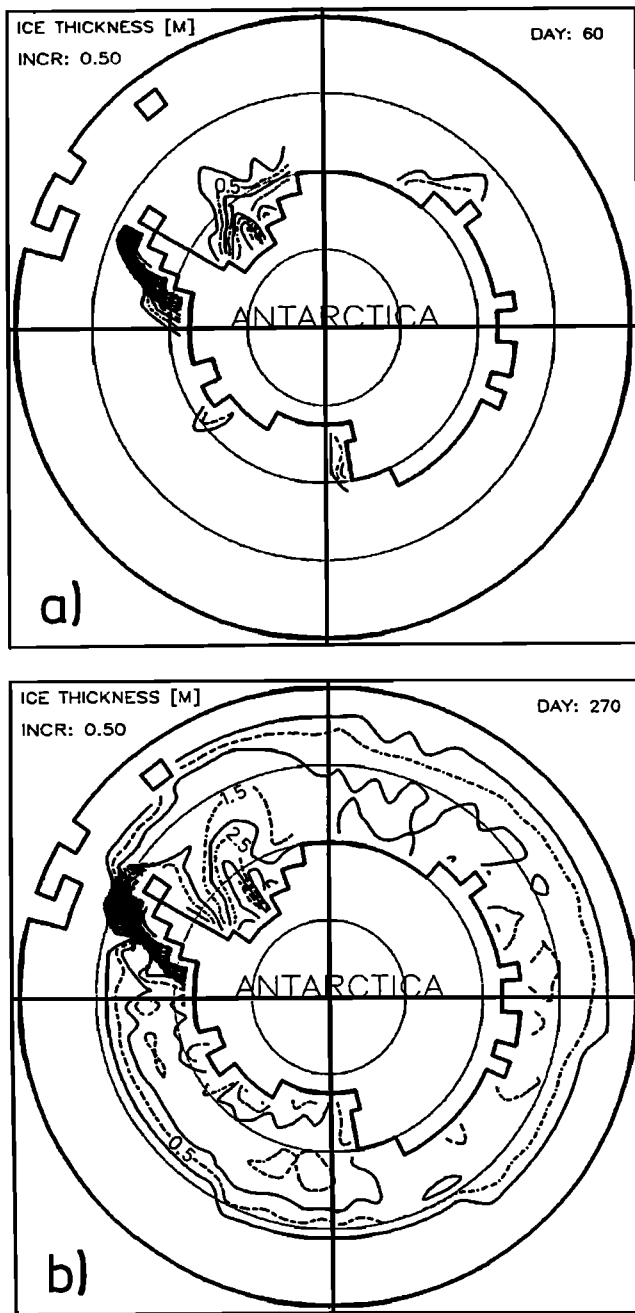
Fig. 15. Ice thickness contours from a run forced with winds from *Hellerman and Rosenstein* [1983] for the days of (*a*) minimum and (*b*) maximum ice extent.

the temperature forcing is not consistent with the humidity forcing, since the dew point temperature is taken from *Taljaard et al.* [1969]. With consistent humidity forcing the differences to the standard run would be even more pronounced.

The warmer temperatures in the *Oort* [1983] data set, representing the period 1963–1973, may result from climatic temperature changes. This is also indicated by *Parkinson and Bindschadler* [1984], who compared the *Taljaard et al.* [1969] data, essentially representative of the period 1931–1960, with data from the Australian Bureau of Meteorology for the years 1973–1981, the latter clearly showing higher average temperatures.

4.3.3. Precipitation. Using the precipitation data from *Jaeger* [1976] (see section 3) instead of those of *Tchernia* [1980] did not significantly affect the seasonal cycle of total ice extent and ice volume. Local differences in ice thickness contours occurred primarily in the area of the Bellingshausen and Amundsen Sea, where the snow depth increased by up to 1 m in the offshore region. Thus, it is important to include not only variable snow thickness in the sea ice model, but also reliable precipitation data, which influence the snow thickness distribution.

4.4. Stochastically Frced Eperiments

Long time series of daily atmospheric data are presently not available. Therefore, experiments have been performed where daily variability was introduced by varying the wind forcing stochastically. Since mean monthly standard deviations of daily winds at the surface are not included in the *Taljaard et al.* [1969] data set, those variables were extracted from the global analysis of *Oort* [1983]. For each grid cell a wind forcing with daily fluctuations was constructed by adding to the *Taljaard et al.* [1969] monthly mean winds stochastically generated u and v components. These fluctuations are horizontally uncorrelated and have a Gaussian distribution with zero mean, and variances equal to those determined by *Oort* [1983]. The resulting winds were used to determine the fluxes of momentum, and sensible and latent heat.

The seasonal cycles of ice extent and effective ice area for this experiment are shown in Figure 19 (heavy lines). The winter ice extent has significantly increased by 4×10^6 km^2 for all three categories. Additionally the winter maximum occurs about 3 weeks earlier as compared to the standard run.

These modifications of the ice-covered area are primarily due to the increased variability of the surface heat fluxes, which is demonstrated in the following experiment (Figure 20, heavy lines), where the wind fluctuations are superimposed only in the dynamic part of the model (momentum fluxes), whereas monthly mean winds are adopted to calculate the fluxes of sensible and latent heat. Now the ice extent is slightly reduced during the winter season, compared to the standard results, especially for the high ice concentration.

Comparing the seasonal variation of the ice volume for these two experiments with the standard run (Figure 21), it is obvious that the stochastic momentum fluxes increase the ice volume by a similar amount as the stochastic heat fluxes. This is the result of an interaction of the dynamics and thermodynamics. The wind fluctuations, which do not increase the ice extent, create ice ridges in convergent regions and open water in divergent areas. Ice ridging itself represents a redistribution of sea ice and does not affect the total ice volume. The open water, on the other hand, is in wintertime rapidly closed by new ice formation, leading to an icrease in ice volume.

The strong influence of the stochastic wind variations on the evaluation of the atmospheric turbulent heat fluxes in the model is primarily due to the fact that at grid cells with weak monthly winds (vector wind) the variability superimposed on the u and v components raises the mean wind speed (scalar wind) which increases the mean heat fluxes and generally causes an increased heat loss to the atmosphere.

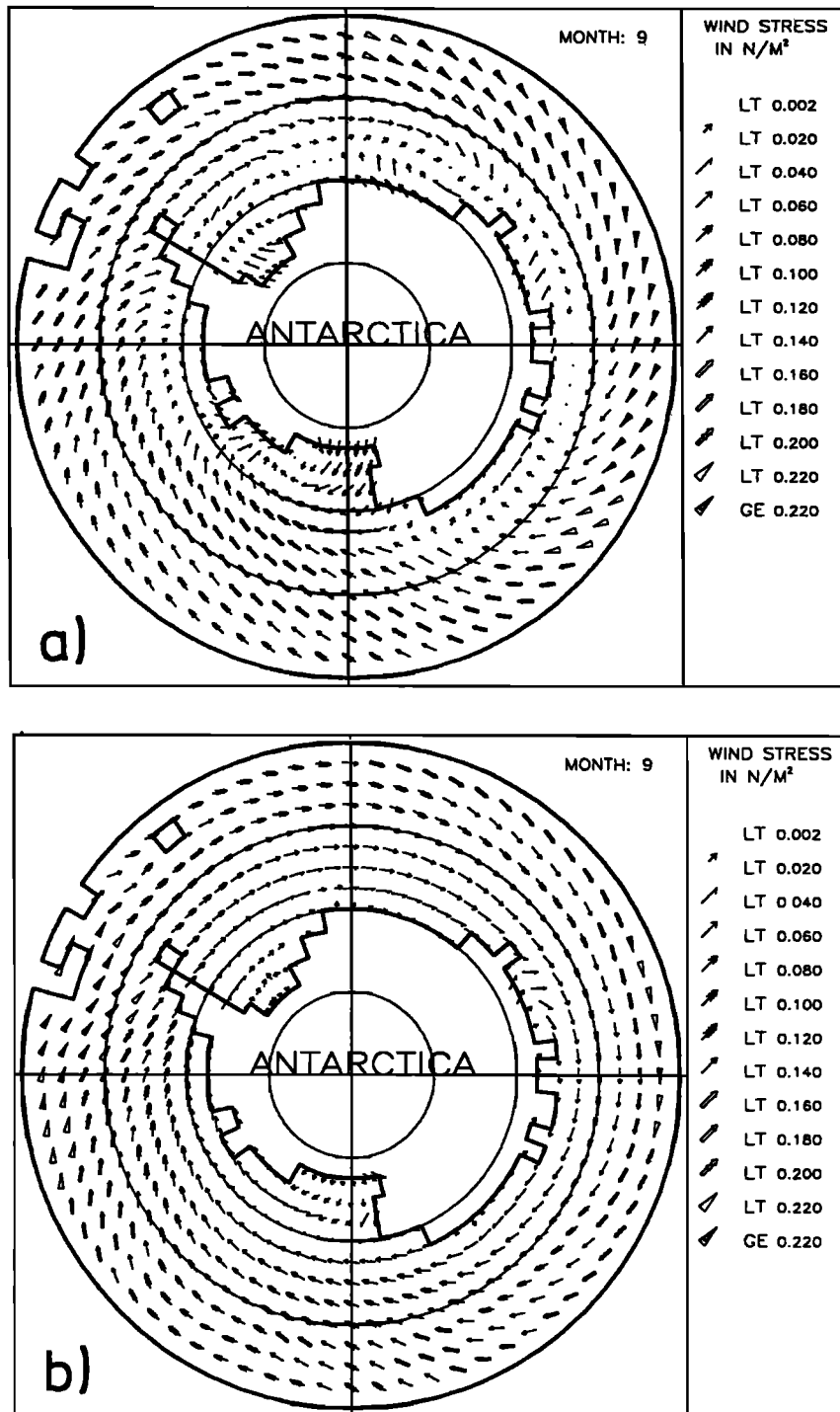As the time resolution of the atmospheric forcing used

Fig. 16. Mean September wind stress derived from (a) the *Taljaard et al.* [1969] geostrophic winds and (b) surface wind stress data according to *Hellerman and Rosenstein* [1983], both interpolated to the model grid. LT and GE denote "less than" and "greater than or equal to," respectively.

with sea ice models is modified, usually only those parameters associated with the momentum flux, such as the drag coefficient [*Parkinson and Washington*, 1979] or the ice strength [*Hibler and Ackley*, 1983], are adjusted. The results presented here imply that the heat flux parameterization should also be considered (see also *Oberhuber* [1988]). Additionally, the transfer coefficients should be determined separately for each grid cell and time step, depending on the

various conditions of the sea ice and the lower atmosphere [e.g., *Stössel*, 1985].

5. CONCLUSIONS

A dynamic-thermodynamic sea ice model with a prognostic snow cover description has been coupled to a prognostic mixed layer-pycnocline model and applied to the Southern
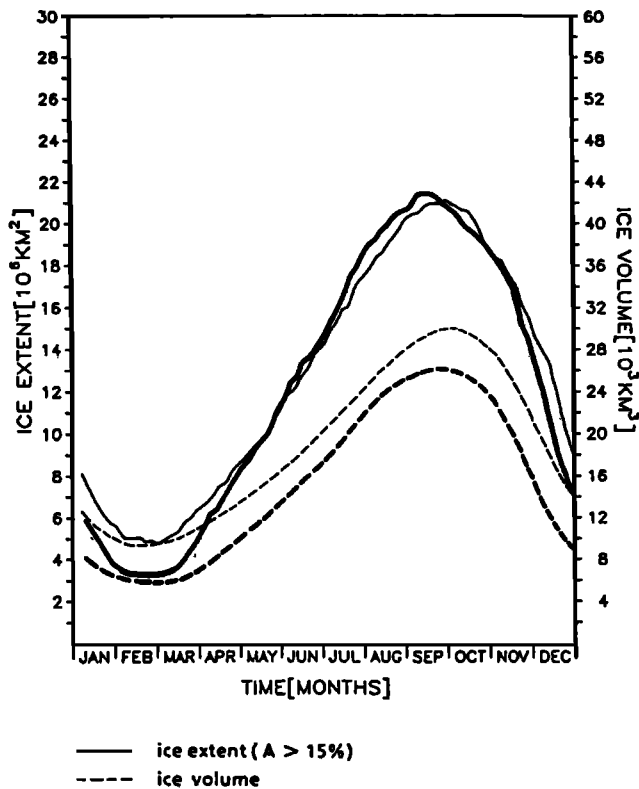
Fig. 17. Seasonal cycles of ice extent and ice volume from a simulation forced with air temperatures from *Oort* [1983] (heavy lines) and the standard experiment (thin lines).

Fig. 18. Ice thickness contours from a run forced with air temperatures from *Oort* [1983] for the (a) minimum and (b) maximum ice extent.

Ocean. Using climatological forcing fields this model reproduced the essential large-scale features of the Antarctic ice pack.

The seasonal cycle of ice extent defined by the 15% compactness contour lines agrees with satellite data in magnitude as well as in phase. The areal distribution of ice thickness together with the locations of coastal polynyas is consistent with the few existing ground truth observations, keeping in mind that the model represents the mean ice thickness averaged over leads, level ice, and ridges.

Compared to the results of *Parkinson and Washington* [1979], the thickness pattern differs considerably, due to the more sophisticated sea ice rheology in the present model. Discrepancies are also apparent in the seasonal cycle of ice volume [*Parkinson and Bindschadler*, 1984], which is about half the magnitude of our standard result.

The present model experiments indicate that sea ice dynamics are essential to describe the pronounced seasonal cycle of ice extent observed in the Southern Ocean. Sea ice is formed near the continent and drifts into northern (warmer) regions, where it melts. Neglecting sea ice dynamics, the large seasonal cycle of ice extent can only be achieved by neglecting additionally mixed layer dynamics and by specifying an unrealistic large constant oceanic heat flux to melt the ice in summer.

The effect of the prognostic mixed layer is apparent in the geographical distribution of the mixed layer depth, which is highly variable in space and time. There are deep mixed layers in the divergent drift regions close to the continent (coastal polynyas), where deep water production takes place due to brine rejection. Similarly the oceanic heat flux
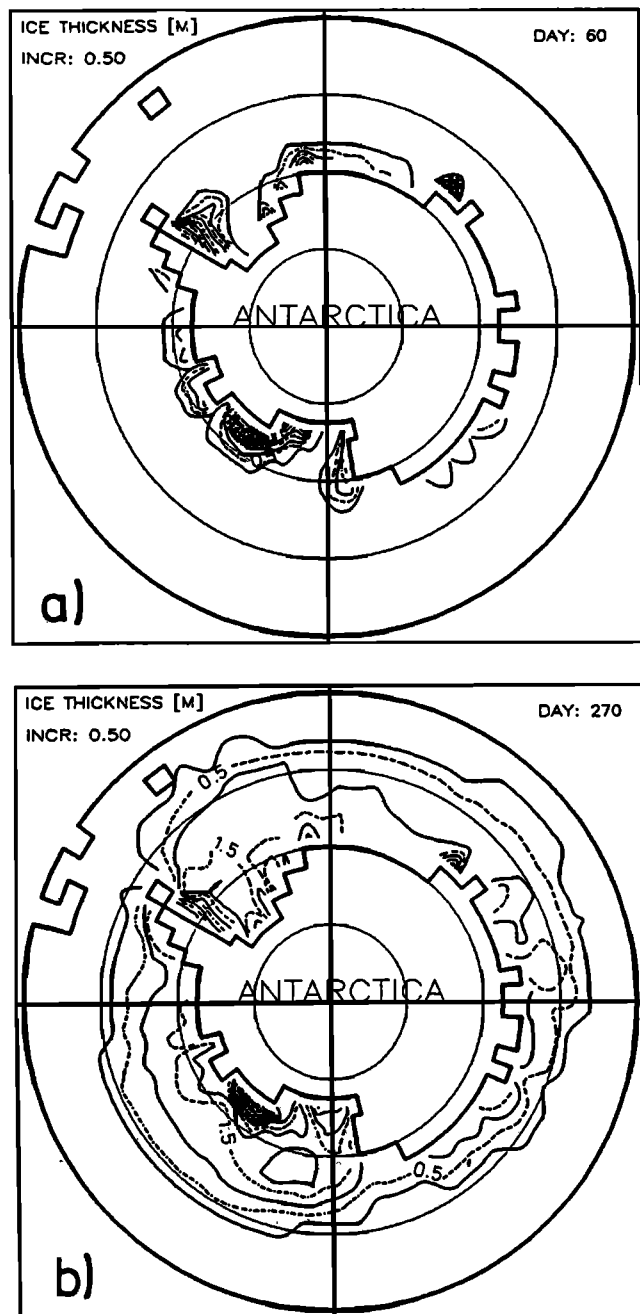
reaches maximum values in wintertime at these locations and at the advancing ice edge during fall and early winter.

The ice velocities are realistically represented, too, although regionally somewhat too low compared to observations. This is presumably due to the coarse resolution of the model, where averaging over one grid cell leads to lower ice velocities. Additionally, the use of monthly mean geostrophic wind forcing might need a more precise determination of the corresponding drag coefficient.

The inclusion of a prognostic snow layer is important for sea ice modeling, especially in the Southern Ocean, where level ice thicknesses usually vary between 0.5 and 1.0 m. Since snow has about 3 times the insulation effect of sea ice,

—— ice extent (A > 15%)
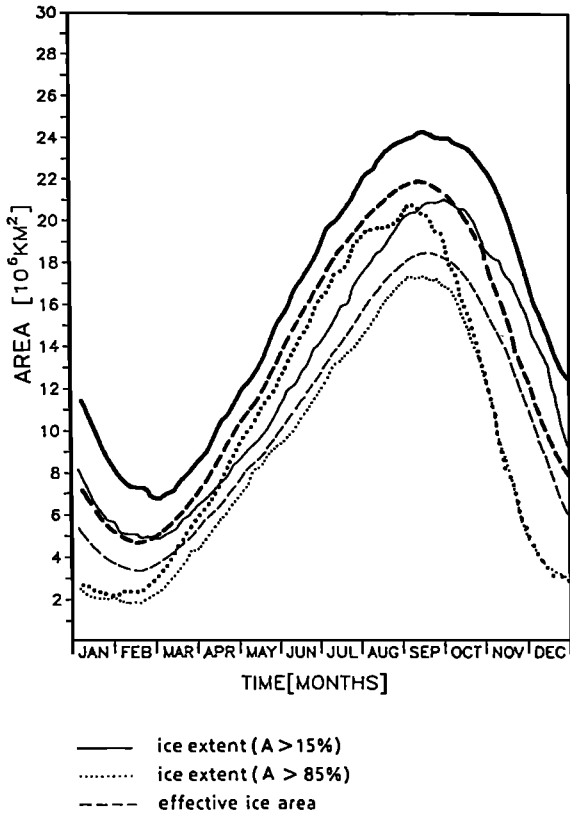··········· ice extent (A > 85%)
———— effective ice area

Fig. 19.   Seasonal cycles of ice extent and effective ice area from a simulation forced by stochastically varying wind fields applied to the dynamic as well as to the thermodynamic part of the model (heavy lines) and from the standard experiment (thin lines).
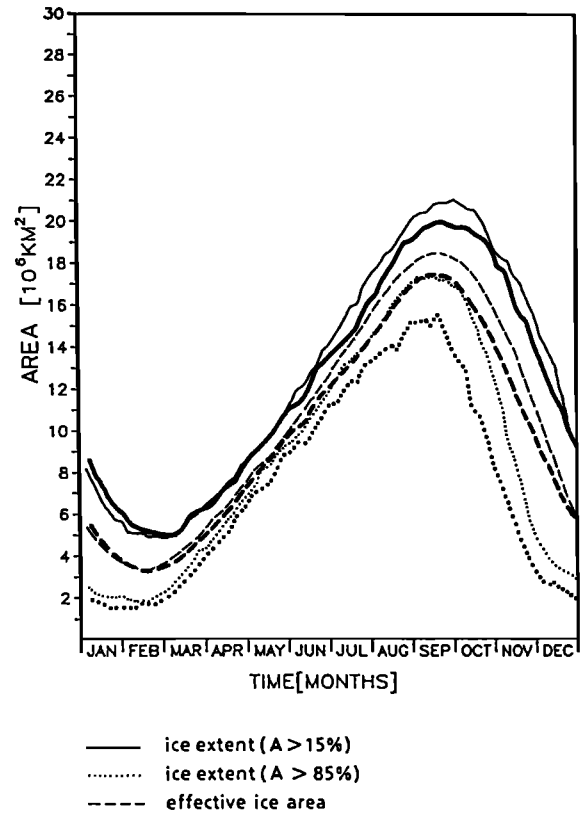

—— ice extent (A > 15%)
··········· ice extent (A > 85%)
———— effective ice area

Fig. 20.   Seasonal cycles of ice extent and effective ice area from a simulation forced by stochastically varying wind fields applied to the dynamic part of the model (momentum flux) (heavy lines) and from the standard run experiment (thin lines).

the precise specification of the snow thickness is most crucial for the determination of the growth rates of sea ice. Apart from the problem of specifying correct snowfall rates, the sea ice model should, in the future, also be coupled to a more sophisticated snow model, incorporating at least variability of snow density, of snow conductivity, of snow albedo, and of snow thickness, all depending on metamorphic processes [Leppäranta, 1983; Stössel, 1985]. As observed by Wadhams et al. [1987], snow ice and slush formation should be considered, too.

Mean geostrophic ocean currents exert little influence on ice drift, implying that the wind is the main driving force for the sea ice motion.

Sensitivities to the choice of the numerical parameters h_0 and P^* which represent the rate that leads close under freezing conditions and ice strength, respectively, suggest that they should be carefully tuned, when more reliable data of areal ice compactnesses (e.g., synthetic aperture radar images), and more ice thickness and velocity measurements, especially in the regions of the western Weddell Sea, the eastern Ross Sea, and the Amundsen Sea, are available.

The addition of daily variability in the wind fields has a strong effect on ice volume and ice extent depending on whether the variability is applied to the dynamic part of the model only or to the full model, i.e., including atmospheric turbulent heat fluxes. Hence, a change from daily wind forcing to monthly mean wind forcing would not only require a change of the drag coefficient but also of the transfer coefficient within the bulk aerodynamic formulas.
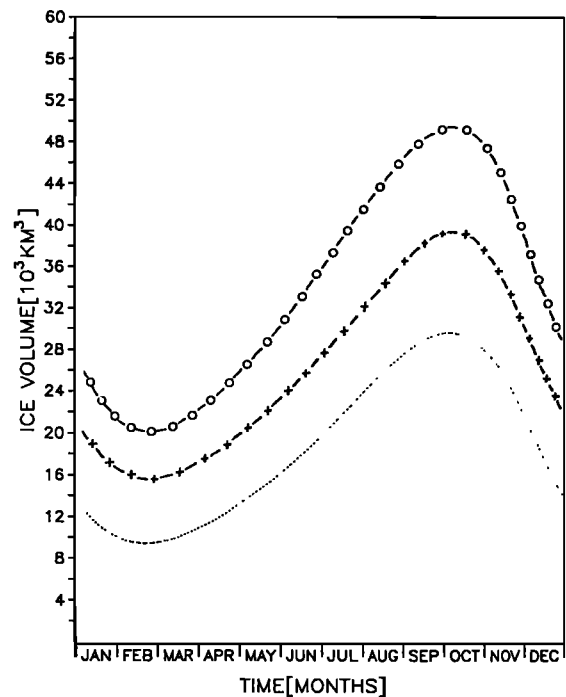

Fig. 21.   Seasonal cycles of ice volume from the standard experiment (dotted lines) and from two stochastically forced runs: with wind variability applied to the dynamic plus the thermodynamic part of the model (circles) and to the dynamic part of the model only (crosses).

The experiments with alternative forcing indicate that the quality of the model results is most sensitive to the forcing fields (especially the winds). Since pure data analyses are crucial as long as the sampling grid is coarse, it seems to be adequate to improve the atmospheric forcing by employing data from operational numerical weather prediction analysis which are a blend of real-time data and forecast values from the previous assimilation time step. Since the surface values are somewhat predetermined, depending on the specified lower boundary conditions (e.g., whether there is sea ice or open water), it seems appropriate to use the forcing from the 850 hPa level. This can be done by coupling the sea ice model to a one-dimensional atmospheric boundary layer model [Koch, 1988], where all surface forcing variables are calculated as functions of the stability of the boundary layer, which in turn is determined by the actual ice condition predicted by the sea ice model.

REFERENCES

Arakawa, A., and V. R. Lamb, Computational design of the basic dynamical processes of the UCLA general circulation model, in *Methods in Computational Physics*, vol. 17, pp. 173–265, Academic, San Diego, Calif., 1977.

Budd, W. F., The southern hemisphere circulation of atmosphere, ocean and sea ice, Report of the Second Session of the Working Group on Sea Ice and Climate, *Tech. Doc. 127*, pp. 47–52, World Meteorol. Organiz., Geneva, 1987.

Crowley, T. J., and C. L. Parkinson, Late Pleistocene variations in Antarctic sea ice, II, Effect of interhemispheric deep-ocean heat exchange, *Clim. Dyn.*, *3*, 93–103, 1988.

Gordon, A. L., and T. Baker, Objective contouring and the grid point data set, in *Southern Ocean Atlas*, chap. 2, pp. 15–29, Columbia University Press, New York, 1982.

Hellerman, S., and M. Rosenstein, Normal monthly wind stress over the world ocean with error estimates, *J. Phys. Oceanogr.*, *13*, 1093–1104, 1983.

Hibler, W. D., III, A dynamic thermodynamic sea ice model, *J. Phys. Oceanogr.*, *9*, 815–846, 1979.

Hibler, W. D., III, The role of sea ice dynamics in modeling CO_2 increases, in *Climate Processes and Climate Sensitivity, Geophys. Monogr. Ser.*, vol. *29*, edited by J. E. Hansen and T. Takahashi, pp. 238–253, AGU, Washington, D. C., 1984.

Hibler, W. D., III, and S. F. Ackley, Numerical simulation of the Weddell Sea pack ice, *J. Geophys. Res.*, *88*, 2873–2887, 1983.

Jaeger, L., Monatskarten des Niederschlags für die ganze Erde, *Ber. Dtsch. Wetterdienstes*, *139*, 1–38, 1976.

Koch, C., A coupled sea ice–atmospheric boundary layer model, 1, Description of the model and 1979 standard run, *Beitr. Phys. Atmos.*, *61* (4), 344–354, 1988.

Lemke, P., A coupled one-dimensional sea ice–ocean model, *J. Geophys. Res.*, *92*, 13,164–13,172, 1987.

Lemke, P., E. W. Trinkl, and K. Hasselmann, Stochastic dynamic analysis of polar sea ice variability, *J. Phys. Oceanogr.*, *10*, 2100–2120, 1980.

Lemke, P., W. B. Owens, and W. D. Hibler III, A coupled sea

ice–mixed layer–pycnocline model for the Weddell Sea, *J. Geophys. Res.*, this issue.

Lepparanta, M., A growth model for black ice, snow ice and snow thickness in subarctic basins, *Nord. Hydrol.*, *14*, 59–70, 1983.

Loewe, P., The ECMWF-T 21 atmospheric GCM: A qualified contender for a coupled climate model including sea ice dynamics?, in *Large Scale Atmospheric Modelling*, rep. 7, *Climate Simulations With the ECMWF T21-Model in Hamburg*, part III, *Diagnosis of Response Experiments*, edited by G. Fischer, pp. 79–123, University of Hamburg, Hamburg, Federal Republic of Germany, 1989.

Oberhuber, J. M., An atlas based on the "COADS" data set: The budgets of heat, buoyancy and turbulent kinetic energy at the surface of the global ocean, *Rep. 15*, Max-Planck-Inst. für Meteorol. Hamburg, Federal Republic of Germany, 1988.

Oort, A. K., Global atmospheric circulation statistics, 1958–1973, *Prof. Pap. 14*, 180 pp., Natl. Oceanic and Atmos. Admin., U.S. Dep. of Commerce, Rockville, Md., 1983.

Owens, W. B., and P. Lemke, Sensitivity studies with a sea ice–mixed layer–pycnocline model in the Weddell Sea, *J. Geophys. Res.*, this issue.

Parkinson, C. L., and R. A. Bindschadler, Response of Antarctic sea ice to uniform atmospheric temperature increases, in *Climate Processes and Climate Sensitivity, Geophys. Monogr. Ser.*, vol. 29, edited by J. E. Hansen and T. Takahashi, pp. 254–264, AGU, Washington, D. C., 1984.

Parkinson, C. L., and W. M. Washington, A large-scale numerical model of sea ice, *J. Geophys. Res.*, *84*, 311–337, 1979.

Stössel, A., Thermodynamic calculations of ice production in the northern Baltic proper, *Dtsch. Hydrogr. Z.*, *38*, 261–284, 1985.

Stowe, L. L., H. Y. M. Yeh, T. F. Eck, C. G. Wellemeyer, H. L. Kyle, and the Nimbus-7 Cloud Data Processing Team, Nimbus-7 global cloud climatology, II, First year results, *J. Clim.*, 2 (7), 671–709, 1989.

Taljaard, J. J., H. van Loon, H. L. Crutcher, and R. L. Jenne, Climate of the upper air, I, Southern hemisphere, vol. 1, Temperatures, dew points and heights at selected pressure levels, *Rep. NAVAIR 50-1C-55*, 135 pp., U.S. Naval Weather Service, Washington, D. C., 1969.

Tchernia, P., *Descriptive Regional Oceanography*, Pergamon, New York, 1980.

van Loon, H., Cloudiness and precipitation in the southern hemisphere, in Meteorology of the Southern Hemisphere, *Meteorol. Monogr.*, *13*, 101–111, 1972.

van Ypersele, J.-P., A numerical study of the response of the Southern Ocean and its sea ice to a CO_2-induced atmospheric warming, Ph.D. thesis, 146 pp., Fac. des Sci., Univ. Cath. de Louvain, Louvain la Neuve, Belgium, 1986.

Wadhams, P., M. A. Lange, and S. F. Ackley, The ice thickness distribution across the Atlantic sector of the Antarctic Ocean in midwinter, *J. Geophys. Res.*, *92* (C13), 14,535–14,552, 1987.

Woodruff, S. D., R. J. Slutz, R. L. Jenne, and P. M. Streurer, A comprehensive ocean-atmosphere data set, *Bull. Am. Meteorol. Soc.*, *68*, 1239–1250, 1987.

Wright, P., An atlas based on the "COADS" data set: Fields of mean wind, cloudiness and humidity at the surface of the global ocean, *Rep. 14*, Max-Planck-Inst. für Meteorol., Hamburg, Federal Republic of Germany, 1988.

Zwally, H. J., J. C. Comiso, C. L. Parkinson, F. D. Carsey, W. J. Campbell, and P. Gloersen, Antarctic sea ice 1973-1976: Satellite passive - microwave observations, *NASA Spec. Publ., SP - 459*, 1–206, 1983.

P. Lemke, Alfred Wegener Institute for Polar and Marine Research, Am Handelshafen 12, D-2850 Bremerhaven, Federal Republic of Germany.

W. B. Owens, Woods Hole Oceanographic Institution, Woods Hole, MA 02543.

A. Stössel, Max-Planck-Institut für Meteorologie, 2000 Hamburg 13, Federal Republic of Germany.